Long-lived population inversion in resonantly driven excitonic antiferromagnet

Jacob A. Warshauer,[1] Huyongqing Chen,[1] Daniel Alejandro Bustamante Lopez,[1] Qishuo Tan,[2] Jing Tang,[2] Xi Ling,[2,3,4] and Wanzheng Hu[1,3,4,*]

[1] *Department of Physics, Boston University, 590 Commonwealth Avenue, Boston, MA 02215, USA*
[2] *Department of Chemistry, Boston University, 590 Commonwealth Avenue, Boston, MA 02215, USA*
[3] *Division of Materials Science and Engineering, Boston University, 590 Commonwealth Avenue, Boston, MA 02215, USA*
[4] *Photonics Center, Boston University, 8 Saint Mary's St., Boston, MA 02215, USA*

Van der Waals magnets are an emerging material family for investigating light-matter interactions and spin-correlated excitations. Here, we report the discovery of a photo-induced state with a lifetime of 17 ps in the van der Waals antiferromagnet $NiPS_3$, which appears exclusively with resonant pumping at 1.476 eV in the antiferromagnetic state. The long-lived state comes with a negative photoconductivity, a characteristic optical response of population inversion. Our findings demonstrate a promising pathway to potentially achieve long-lived lasing at terahertz frequencies in reduced dimensions.

Excitons are electron-hole pairs bound by Coulomb attraction that broadly exist in condensed matter systems. Optically driven excitonic systems host a vast range of compelling features, including intraexcitonic resonances[1], the Hubbard exciton[2], exciton sensing of coherent magnon[3], and spin-polarized spatially indirect exciton[4]. The beauty of rich excitonic physics, however, is eventually limited by the exciton's lifetime before the electron-hole recombination. Long-lived excitons are appealing for the realization of exciton condensation[5–7] and optoelectronic device applications[8], making materials with long-lived excitonic states highly sought after.

Van der Waals magnets are an emerging material family for investigating light-matter interactions and spin-correlated excitations[9–19]. The discovery of an ultra-narrow photoluminescence (PL) peak in the antiferromagnetic material $NiPS_3$, identified as a spin-correlated exciton state, opening up novel opportunities to study coherent many-body excitons[9, 13, 20, 21]. The 330-μeV linewidth of the exciton peak in $NiPS_3$[10, 11] is significantly narrower than the typical sub-10 meV exciton linewidth found in two-dimensional semiconductors[22–24], which makes $NiPS_3$ an ideal platform to investigate the exciton dynamics. Apart from the ultra-narrow exciton linewidth, the other fascinating character is the connection between the exciton and magnetic ordering. The exciton PL peak appears only in the antiferromagnetic phase[10–12] and displays a splitting under the application of an in-plane magnetic field[20, 25]. The exciton peak is highly anisotropic with a temperature dependence following the in-plane magnetic susceptibility anisotropy[11], and the exciton dispersion follows closely the double-magnon dispersion[26], indicating a close relationship between the exciton and the magnetic order. Despite extensive interest in the ultra-narrow spin-correlated exciton, there are no studies on resonant driving at exciton levels in $NiPS_3$ or other van der Waals magnets in this family.

* wanzheng@bu.edu

Here we use resonant optical excitation to populate the spin-correlated exciton state in the antiferromagnet $NiPS_3$. We probe the charge dynamics using time-resolved terahertz (THz) spectroscopy, which has played a major role in probing intra-exciton transitions[1, 2, 27]. By tuning the pump photon energy to two of the excitonic features and an energy above the absorption onset, we identify a distinct state tied to the spin-correlated exciton with a lifetime of 17 ps. Further, we show that the long-lived state exhibits a negative photoconductivity over the entire THz probe range, which we attribute to population inversion involving the excitonic ground state.

Millimeter-thick bulk single crystals of $NiPS_3$ with a Néel temperature (T_N) of 155 K were grown by the chemical vapor transport method[10]. Within individual $NiPS_3$ layers, the spins on the Ni lattice are antiferromagnetically ordered along the b axis and form a zigzag pattern along the a axis. Highly anisotropic exciton features develop in the antiferromagnetic state[9–12]. Peak I, seen at 1.476 eV in the optical absorption (Figure 1(a)), is a spin-orbit-entangled exciton[9, 21]. This exciton, probed by the PL, is highly polarized with the largest signal along the b axis[10], where the spins are antiferromagnetically ordered (Figure 1(a) inset). The second sharp optical transition (peak II in Fig.1(a)) is 22 meV above peak I and is identified as a magnon sideband of the exciton peak I[9, 28].

Optical excitation at three selected frequencies was used to drive $NiPS_3$ out of equilibrium: (1) resonant pumping of the exciton at 1.476 eV, (2) resonant pumping of the magnon sideband of the exciton at 1.494 eV, and (3) off-resonant pumping at 1.61 eV which is slightly above the absorption onset[29] at 7 K. The shaded peaks in Fig. 1(a) are the spectra of three excitation energies used in this study. The pump beam polarization was parallel to the a axis of $NiPS_3$. We performed time-resolved THz spectroscopy to probe the dynamics of the driven state. The THz probe reached the sample at normal incidence in reflection geometry (Fig.1(b)). The probe polarization was set parallel to the b axis of $NiPS_3$. Further

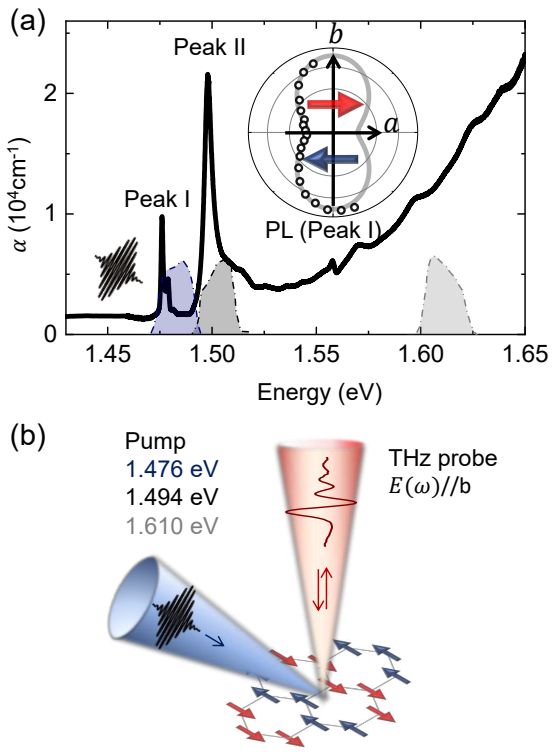

FIG. 1. (a) Equilibrium absorption coefficient α at 4 K (data from Ref.[9]), and three excitation spectra used in this study (shaded peaks). (Inset) The PL intensity maximizes along the b axis, where the spins on the Ni lattice are antiferromagnetically ordered. (b) The transient state was probed by THz pulses using normal incidence reflection.

details on the pump-probe measurement can be found in the Supplemental Material [30].

We first present the spectrally-integrated transient dynamics. Figure 2(a) shows the time-domain pump-probe response at 7 K with resonant excitation at peak I. Here, ΔE is the pump-induced change in the reflected THz field at the peak value, and E is the peak value of the equilibrium THz waveform. After excitation, the pump-probe signal reaches maximum and then decreases to negative values, remaining negative for several tens of picoseconds. Fitting over an extended time window (Fig. S3) reveals two time constants of the transient response. The sign-changing response is short-lived with a lifetime of 0.2 ps, which is likely the time of exciton formation[37]. The long-lived negative signal has a lifetime of 17 ps, which is on the same order as the lifetime of the exciton[10, 11, 38]. In addition, an oscillatory response is seen with a frequency of 1.2 THz (5.0 meV). This corresponds to an out-of-plane magnon according to the solutions to the Landau–Lifshitz–Gilbert equations (Supplemental Material section S7 [30]) and agrees with the magnon frequency observed by Raman scattering[20] and THz emission[15, 39]. The lifetime of the magnon signal is 70 ps according to our calculation, which fits the THz time trace (Fig. 2(a) and Fig. S3).

The negative pump-probe response with a long lifetime is unique to resonant pumping at peak I. As illustrated in Fig. 2(b), when pumping at peak II (1.494 eV) or above the absorption edge (1.610 eV) at the same base temperature of 7 K, the pump-probe signals are nearly identical. Only a positive response is seen, and the dynamics are much shorter lived with a lifetime on the order of 3 ps for both cases. A positive $\Delta E/E$ is not surprising for optically excited insulator, as the pump photons above the absorption onset can create hot carriers which enhance material's reflectivity at THz frequencies. In the antiferromagnetic state, pumping away from peak I also leads to a significant reduction in the magnon signature, similar to case of antiferromagnetic NiO[40].

We then demonstrate the temperature evolution of the pump-probe dynamics. Figure 2(c) shows a set of pump-probe overlap scans at various temperatures across T_N = 155 K (see Fig. 2(d)) with the same excitation energy of 1.476 eV. With increasing temperature, the exciton peak red-shifts and broadens considerably at 70 K, before nearly disappearing at 130 K[9–12]. Accordingly, the suppression in $\Delta E/E$ significantly weakens from 7 K to 70 K, and it is barely recognizable at 130 K. Additionally, the absorption onset also redshifts continuously with increasing temperature so that at room temperature 1.476 eV is above the absorption onset[29]. Consistently, a positive $\Delta E/E$ is seen at room temperature with 1.476 eV pumping, similar to the off-resonant case at 7 K (Fig. 2(b)).

We now investigate the unique long-lived state by the frequency-resolved optical response. Figure 3(a-d) shows the time evolution of the light-induced change in the complex optical conductivity, defined as $\Delta\sigma(\omega) = \sigma(\omega)^{\text{transient}} - \sigma(\omega)^{\text{equilibrium}}$. At the maximum response (Fig. 3(a)), $\Delta\sigma_1(\omega)$ is positive at low energies and becomes negative in between 6 and 10 meV, while $\Delta\sigma_2(\omega)$ is positive over the entire energy window. At later time delays, $\Delta\sigma_1(\omega)$ remains negative from 4 to 10 meV, while $\Delta\sigma_2(\omega)$ remains positive (Fig. 3(b-d)). The real and imaginary part of optical conductivity can be fit simultaneously with a Drude term plus a Lorentz component with a negative amplitude. A typical fit is shown in Fig. 3(e). The Drude term gives a positive contribution to $\Delta\sigma_1(\omega)$ for all frequencies, and the inverted Lorentz term brings $\sigma_1(\omega)$ to negative values. Varying the pump-probe time delay, the oscillator strengths for the Drude and inverted Lorentz terms change with different rates, while their widths remain constant (γ^{Drude}=1.5 meV and γ^{Lorentz}=5 meV). Figure 3(f) plots the time evolution of the Drude and Lorentz oscillator strengths. The Drude oscillator strength ω_{pD}^2 can be fit with a single exponential decay with a time constant of 2.4 ps. The inverted Lorentz oscillator strength ω_{pL}^2 reaches maximum at 2 ps then decays with 2 ps and 15 ps time constants. The transient spectral weight, defined as $\Delta SW = \frac{120}{\pi}\int_{\omega_1}^{\omega_2}\Delta\sigma_1(\omega)\,d\omega$, in the range between 4 and 10 meV (open squares in Fig. 3(f)) qualitatively follows the exponential fit for the spectrally-integrated response

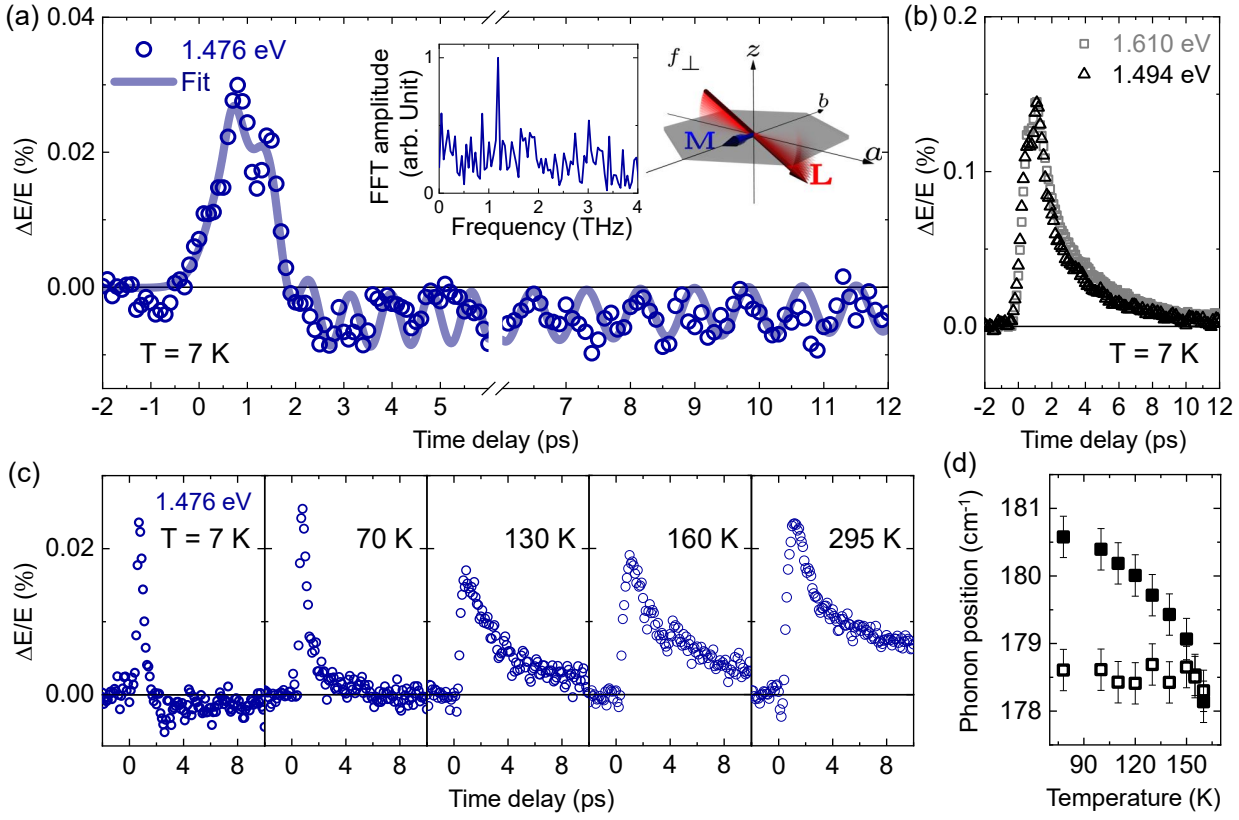

FIG. 2. (a) Pump-induced change in the THz electric field ($\Delta E/E$) with resonant pumping at peak I at 7 K. $\Delta E/E$ quickly switches sign and remains negative for several tens of picosecond. Meanwhile, an oscillation with a frequency of 1.2 THz (left inset) is seen, corresponding to a magnon mode (right inset). (b) At 7 K, when the pump frequency is tuned to peak II (1.494 eV, triangles) or to above the absorption onset (1.610 eV, squares), $\Delta E/E$ is short lived and remains positive. (c) Temperature evolution of $\Delta E/E$ with 1.476 eV pumping. (d) Néel temperature (155 K) characterized by the splitting of a 180-cm^{-1} Raman phonon along the parallel (solid squares) and cross (open squares) polarization geometry[36].

presented in Fig. 2(a). A suppression in spectral weight as a result of the negative $\Delta\sigma_1$ is seen up to 30 ps. The frequency-resolved optical response verifies that the overall pump-probe dynamics comes from two contributions with different time scales. We are particularly interested in the inverted Lorentz term, which is a non-thermal response.

This unique non-thermal response disappears when pumping away from peak I. Figure 3(g) shows the transient change of the complex optical conductivity with pumping at peak II, which is about 20 meV above peak I. In this configuration, $\Delta\sigma_1(\omega)$ remains positive over the entire energy window, decreasing at higher probe energies, while $\Delta\sigma_2(\omega)$ peaks near 7 meV. This is characteristic of a free-carrier Drude response (Fig. 3(h))[41]. Similar Drude behavior is seen for 1.476 eV pumping at room temperature (Figure S5) where the exciton disappears and the pump energy is above the absorption edge. These frequency-resolved responses agree with the positive $\Delta E/E$ dynamics as shown in Fig. 2(b), thereby verifying the high sensitivity of the transient state to the excitation photon energy: as soon as the excitation energy is at or above the absorption onset, the Drude response dominates.

We now explore possible origins of the long-lived state with resonant pumping at peak I. As the negative $\Delta\sigma_1(\omega)$ is only observed with the resonant excitation of peak I, and the lifetime of this state is comparable to that of the exciton lifetime[10, 11, 38], this response must come from optical population of the 1.476 eV exciton level. A negative $\Delta\sigma_1(\omega)$ has been observed in other exciton systems and was interpreted as stimulated emission from population inversion of intraexcitonic levels[27]. At first, a population inversion is formed by resonant excitation by the optical pump, and then the THz probe photons stimulate a coherent emission similar to the process of lasing. In our case, the reflected THz peak field (Fig. 2(a)) encompasses multiple contributions including a coexistent Drude term. We therefore focus on the negative $\Delta\sigma_1(\omega)$ in the following discussion.

The population inversion picture is further verified by the incident pump fluence dependence of the negative spectral weight, $-\Delta$SW, which follows a threshold-saturation behavior expected for population inversion between excited energy levels, as shown in the inset of Fig. 3(f) and Supplemental Material section S6 [30]. As each

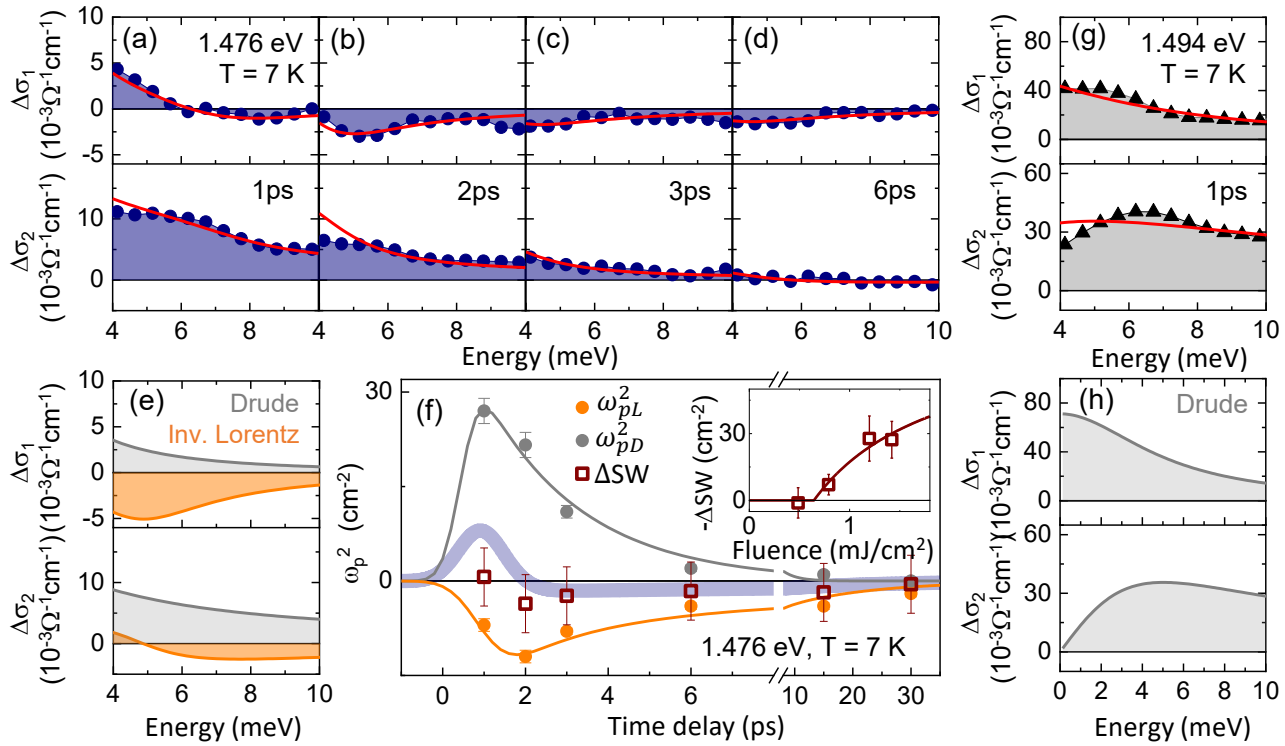

FIG. 3. (a-d) Resonant pumping at the exciton energy (peak I) results in a long-lived transient suppression in σ_1 and an increase in σ_2. The solid circles present the data, and the red curves are fits. (e) The Drude and inverted Lorentz terms used to fit the 2 ps data. (f) Time dependence of the fitting parameters at 7 K with 1.476 eV pumping. ω_{pL}^2 and ω_{pD}^2 represent the oscillator strength of the inverted Lorentz term and the Drude term, respectively. The thin solid lines are exponential decay fits. A global ω_p^2 represented by the optical spectral weight under $\Delta\sigma_1(\omega)$ in between 4 and 10 meV (ΔSW). The thick blue line is a rescaled exponential fit used for $\Delta E/E$. (Inset) Transient change in spectral weight as a function of incident pump fluence at $t = 3ps$. (g) Pumping at peak II results in positive $\Delta\sigma_1$ and $\Delta\sigma_2$ (solid triangles) which can be fit with a single Drude term (red lines). (h) The Drude term used to fit **g** across a broader spectral region.

pump spectrum covers a relatively broad frequency range with respect to the narrow exciton linewidth (see Fig. 1(a)), the exciton state (peak I) can be either the lower or higher level of the population inversion state. Multiple exciton states close to peak I have been predicted by first-principles calculations[42, 43]. Additionally, shoulder peaks at closely spaced energies above the 1.476 eV peak have been observed in photoluminescence and absorption measurements[9]. Therefore, our observation reflects a population inversion involving the 1.476 eV exciton and another nearby exciton level. Note that the inverted Lorentz term in $\Delta\sigma_1(\omega)$ peaks at 5 meV, overlapping with the magnon energy as shown in Fig. 2(a) inset. One may speculate that the negative $\Delta\sigma_1(\omega)$ comes from a magnon-facilitated THz emission; however, this is not likely the case because the suppression in $\Delta\sigma_1(\omega)$ has a much broader energy width than the magnon feature[15].

We briefly comment on other possibilities which can lead to a negative $\Delta\sigma_1(\omega)$. In metallic systems such as graphene, optical excitation leads to a dominant increase in the scattering rate of the existing carriers[44, 45]. Here, $NiPS_3$ is insulating with no free-carrier response at equilibrium. Similarly, we can rule out trion formation as the cause of the negative $\Delta\sigma_1(\omega)$. Trions arise from the pre-existing free carriers bound with the photogenerated excitons[46], but there are no pre-existing free carriers in our case. Finally, although a reduction of the Lorentz oscillator strength of the absorption near 2.2 eV[47] can result in a negative $\Delta\sigma_1(\omega)$ and a positive $\Delta\sigma_2(\omega)$ in the THz range, no significant changes in the reflectivity near 2.2 eV was observed under similar pumping conditions[16]. Further pump-probe studies are needed to investigate the dynamics of the multiple excitonic features near 1.5 eV under resonant excitations.

In conclusion, we discover a long-lived light-induced state with negative photoconductivity in bulk $NiPS_3$ by resonant pumping at the exciton energy. We interpret this as a population inversion state involving the excitonic ground state. Our study provides new insights to understand the nature of the spin-orbit-entangled exciton and the fine optical features nearby, for which limited data and diverse interpretations exist[9, 10, 12, 20, 21, 26, 43]. The long-lived state is unique to resonant pumping at the exciton level, while increasing the pump photon energy by about 20 meV results in short-lived free-carrier response. As the narrow-band optical excita-

tions used in this study are approachable for a wide range of table-top time-resolved techniques and large scale facilities such as femtosecond X-rays from free-electron lasers, our findings open up broad research opportunities to explore long-lived excitonic phases in optically driven nonequilibrium states. In particular, the long lifetime of the spin-orbit-entangled exciton and the exciton-magnon coupling in $NiPS_3$ are appealing for exploring exciton dynamics, exciton condensation and exciton-magnon interactions in light-driven states. Furthermore, since the exciton linewidth in $NiPS_3$ remains narrow down to the trilayer level[10], atomically-thin $NiPS_3$ can serve as a building block for van der Waals heterojunctions or superlattices to potentially achieve long-lived lasing at terahertz frequencies in reduced dimensions.

This material is based upon work supported by the National Science Foundation under Grant No. 1944957. H. C., D. A. B. L. and W. H. acknowledge support from the U.S. Department of Energy, Office of Science, Office of Basic Energy Sciences Early Career Research Program under Award Number DE-SC-0021305. Work by Q. T., J. T. and X. L. were supported by the National Science Foundation (NSF) under Grant No. (1945364) and the U.S. Department of Energy, Office of Science, Basic Energy Sciences under Award DE-SC0021064. Q.T. acknowledges support of the Laursen Graduate Research Award. We acknowledge the helpful discussions with Matteo Mitrano, Yue Cao, Gregory Fiete and Martin Eckstein. We thank Boston University Photonics Center for technical support.

[1] R. A. Kaindl, M. A. Carnahan, D. Hägele, R. Lövenich, and D. S. Chemla, Ultrafast terahertz probes of transient conducting and insulating phases in an electron–hole gas, Nature 423, 734 (2003).

[2] O. Mehio, X. Li, H. Ning, Z. Lenarčič, Y. Han, M. Buchhold, Z. Porter, N. J. Laurita, S. D. Wilson, and D. Hsieh, A Hubbard exciton fluid in a photo-doped antiferromagnetic Mott insulator, Nat. Phys. 19, 1876 (2023).

[3] Y. J. Bae, J. Wang, A. Scheie, J. Xu, D. G. Chica, G. M. Diederich, J. Cenker, M. E. Ziebel, Y. Bai, H. Ren, C. R. Dean, M. Delor, X. Xu, X. Roy, A. D. Kent, and X. Zhu, Exciton-coupled coherent magnons in a 2D semiconductor, Nature 609, 282 (2022).

[4] R. Mori, S. Ciocys, K. Takasan, P. Ai, K. Currier, T. Morimoto, J. E. Moore, and A. Lanzara, Spin-polarized spatially indirect excitons in a topological insulator, Nature 614, 249 (2023).

[5] J. Eisenstein, Exciton Condensation in Bilayer Quantum Hall Systems, Annu. Rev. Condens. Matter Phys. 5, 159 (2014).

[6] A. Kogar, M. S. Rak, S. Vig, A. A. Husain, F. Flicker, Y. I. Joe, L. Venema, G. J. MacDougall, T. C. Chiang, E. Fradkin, J. van Wezel, and P. Abbamonte, Signatures of exciton condensation ina transition metal dichalcogenide, Science 358, 1314 (2017).

[7] S. R. U. Haque, M. H. Michael, J. Zhu, Y. Zhang, L. Windg¨atter, S. Latini, J. P. Wakefield, G.-F. Zhang, J. Zhang, A. Rubio, J. G. Checkelsky, E. Demler, and R. D. Averitt, Terahertz parametric amplification as a reporter of exciton condensate dynamics, Nat. Mater. (2024).

[8] K. F. Mak and J. Shan, Photonics and optoelectronics of 2D semiconductor transition metal dichalcogenides, Nature Photonics 10, 216 (2016).

[9] S. Kang, K. Kim, B. H. Kim, J. Kim, K. I. Sim, J.-U. Lee, S. Lee, K. Park, S. Yun, T. Kim, A. Nag, A. Walters, M. Garcia-Fernandez, J. Li, L. Chapon, K.-J. Zhou, Y.-W. Son, J. H. Kim, H. Cheong, and J.-G. Park, Coherent many-body exciton in van der Waals antiferromagnet $NiPS_3$, Nature 583, 785 (2020).

[10] X. Wang, J. Cao, Z. Lu, A. Cohen, H. Kitadai, T. Li, Q. Tan, M. Wilson, C. H. Lui, D. Smirnov, S. Sharifzadeh, and X. Ling, Spin-induced linear polarization of photoluminescence in antiferromagnetic van der Waals crystals, Nature Materials 20, 964 (2021).

[11] K. Hwangbo, Q. Zhang, Q. Jiang, Y. Wang, J. Fonseca, C. Wang, G. M. Diederich, D. R. Gamelin, D. Xiao, J.-H. Chu, W. Yao, and X. Xu, Highly anisotropic excitons and multiple phonon bound states in a van der Waals antiferromagnetic insulator, Nature Nanotechnology 16, 655 (2021).

[12] D. S. Kim, D. Huang, C. Guo, K. Li, D. Rocca, F. Y. Gao, J. Choe, D. Lujan, T.-H. Wu, K.-H. Lin, E. Baldini, L. Yang, S. Sharma, R. Kalaivanan, R. Sankar, S.-F. Lee, Y. Ping, and X. Li, Anisotropic Excitons Reveal Local Spin Chain Directions in a van der Waals Antiferromagnet, Advanced Materials 35, 2206585 (2023).

[13] F. Dirnberger, R. Bushati, B. Datta, A. Kumar, A. H. MacDonald, E. Baldini, and V. M. Menon, Spincorrelated exciton–polaritons in a van der Waals magnet, Nature Nanotechnology 17, 1060 (2022).

[14] D. Afanasiev, J. R. Hortensius, M. Matthiesen, S. Mañas-Valero, M. Šiškins, M. Lee, E. Lesne, H. S. J. van der Zant, P. G. Steeneken, B. A. Ivanov, E. Coronado, and A. D. Caviglia, Controlling the anisotropy of a van der Waals antiferromagnet with light, Science Advances 7, eabf3096 (2021).

[15] C. A. Belvin, E. Baldini, I. O. Ozel, D. Mao, H. C. Po, C. J. Allington, S. Son, B. H. Kim, J. Kim, I. Hwang, J. H. Kim, J.-G. Park, T. Senthil, and N. Gedik, Excitondriven antiferromagnetic metal in a correlated van der Waals insulator, Nat. Commun. 12, 4837 (2021).

[16] E. Ergeçen, B. Ilyas, D. Mao, H. C. Po, M. B. Yilmaz, J. Kim, J.-G. Park, T. Senthil, and N. Gedik, Magnetically brightened dark electron-phonon bound states in a van der Waals antiferromagnet, Nat. Commun. 13, 98 (2022).

[17] T. T. Mai, K. F. Garrity, A. McCreary, J. Argo, J. R. Simpson, V. Doan-Nguyen, R. V. Aguilar, and A. R. H. Walker, Magnon-phonon hybridization in 2D antiferromagnet $MnPSe_3$, Sci. Adv. 7, eabj3106 (2021).

[18] J.-U. Lee, S. Lee, J. H. Ryoo, S. Kang, T. Y. Kim, P. Kim, C.-H. Park, J.-G. Park, and H. Cheong, Ising- Type Magnetic Ordering in Atomically Thin $FePS_3$, Nano Lett. 16, 7433 (2016).

[19] Q. Tan, W. Luo, T. Li, J. Cao, H. Kitadai, X. Wang, and X. Ling, Charge-transfer-enhanced d–d emission in antiferromagnetic $NiPS_3$, Appl. Phys. Rev. 9, 041406 (2022).

[20] D. Jana, P. Kapuscinski, I. Mohelsky, D. Vaclavkova, I. Breslavetz, M. Orlita, C. Faugeras, and M. Potemski, Magnon gap excitations and spin-entangled optical transition in van derWaals antiferromagnet $NiPS_3$, Phys. Rev. B 108, 115149 (2023).

[21] T. Klaproth, S. Aswartham, Y. Shemerliuk, S. Selter, O. Janson, J. van den Brink, B. Büchner, M. Knupfer, S. Pazek, D. Mikhailova, A. Efimenko, R. Hayn, A. Savoyant, V. Gubanov, and A. Koitzsch, Origin of the Magnetic Exciton in the van der Waals Antiferromagnet $NiPS_3$, Phys. Rev. Lett. 131, 256504 (2023).

[22] J. S. Ross, S. Wu, H. Yu, N. J. Ghimire, A. M. Jones, G. Aivazian, J. Yan, D. G. Mandrus, D. Xiao, W. Yao, and X. Xu, Electrical control of neutral and charged excitons in a monolayer semiconductor, Nat. Commun. 4, 1474 (2013).

[23] F. Cadiz, E. Courtade, C. Robert, G. Wang, Y. Shen, H. Cai, T. Taniguchi, K. Watanabe, H. Carrere, D. Lagarde, M. Manca, T. Amand, P. Renucci, S. Tongay, X. Marie, and B. Urbaszek, Excitonic Linewidth Approaching the Homogeneous Limit in MoS_2-Based van derWaals Heterostructures, Physical Review X 7, 021026 (2017).

[24] J. Wierzbowski, J. Klein, F. Sigger, C. Straubinger, M. Kremser, T. Taniguchi, K.Watanabe, U.Wurstbauer, A. W. Holleitner, M. Kaniber, K. Müller, and J. J. Finley, Direct exciton emission from atomically thin transition metal dichalcogenide heterostructures near the lifetime limit, Scientific Reports 7, 12383 (2017).

[25] X. Wang, Q. Tan, T. Li, Z. Lu, J. Cao, Y. Ge, L. Zhao, J. Tang, H. Kitadai, M. Guo, Y. Li, W. Xu, R. Cheng, D. Smirnov, and X. Ling, Unveiling the spin evolution in van der Waals antiferromagnets via magneto-exciton effects, Nature Communications 15, 8011 (2024).

[26] W. He, Y. Shen, K. Wohlfeld, J. Sears, J. Li, J. Pelliciari, M. Walicki, S. Johnston, E. Baldini, V. Bisogni, M. Mitrano, and M. P. M. Dean, Magnetically propagating Hund's exciton in van der Waals antiferromagnet $NiPS_3$, arXiv:2404.10827v1.

[27] R. Huber, B. A. Schmid, Y. R. Shen, D. S. Chemla, and R. A. Kaindl, Stimulated Terahertz Emission from Intraexcitonic Transitions in Cu_2O, Phys. Rev. Lett. 96, 017402 (2006).

[28] T. Kaneko, Y. Murakami, D. Golež, Z. Sun, and A. J. Millis, Exciton-spin interactions in antiferromagnetic charge-transfer insulators, Phys. Rev. B 108, 205121 (2023).

[29] C.-H. Ho, T.-Y. Hsu, and L. C. Muhimmah, The band-edge excitons observed in few-layer $NiPS_3$, npj 2D Materials and Applications 5, 8 (2021).

[30] See Supplemental Material at **[url]** for further details on experimental methods, data fitting, and theory calculations, which includes Refs. [31–35].

[31] M. Šiškins, M. Lee, S. Mañas-Valero, E. Coronado, Y. M. Blanter, H. S. J. van der Zant, and P. G. Steeneken, Magnetic and electronic phase transitions probed by nanomechanical resonators, Nature Communications 11, 2698 (2020).

[32] D. Fausti, R. I. Tobey, N. Dean, S. Kaiser, A. Dienst, M. C. Hoffmann, S. Pyon, T.Takayama, H. Takagi, and A. Cavalleri, Light-Induced Superconductivity in a Stripe-Ordered Cuprate, Science 331, 189 (2011).

[33] R. D. Guenther and D. Steel, *Encyclopedia of Modern Optics* (Academic Press, San Diego, CA, 2018).

[34] J. T. Verdeyen, *Laser Electronics* (Presntice-Hall, 1995).

[35] A. R. Wildes, J. R. Stewart, M. D. Le, R. A. Ewings, K. C. Rule, G. Deng, and K. Anand, Magnetic dynamics of $NiPS_3$, Phys. Rev. B 106, 174422 (2022).

[36] K. Kim, S. Y. Lim, J.-U. Lee, S. Lee, T. Y. Kim, K. Park, G. S. Jeon, C.-H. Park, J.-G. Park, and H. Cheong, Suppression of magnetic ordering in XXZ-type antiferromagnetic monolayer $NiPS_3$, Nat. Commun. 10, 345 (2019).

[37] P. Steinleitner, P. Merkl, P. Nagler, J. Mornhinweg, C. Schüller, T. Korn, A. Chernikov, and R. Huber, Direct Observation of Ultrafast Exciton Formation in a Monolayer of WSe_2, Nano Letters 17, 1455 (2017).

[38] Y. Li, G. Liang, C. Kong, B. Sun, and X. Zhang, Charge-Transfer-Mediated Exciton Dynamics in Van der Waals Antiferromagnet $NiPS_3$, Adv. Funct. Mater. 2402161 (2024).

[39] C. J. Allington, C. A. Belvin, U. F. P. Seifert, M. Ye, T. Tai, E. Baldini, S. Son, J. Kim, J. Park, J.-G. Park, L. Balents, and N. Gedik, Distinct Optical Excitation Mechanisms of a Coherent Magnon in a van der Waals Antiferromagnet, arXiv:2402.17041v1.

[40] D. Bossini, M. Pancaldi, L. Soumah, M. Basini, F. Mertens, M. Cinchetti, T. Satoh, O. Gomonay, and S. Bonetti, Ultrafast Amplification and Nonlinear Magnetoelastic Coupling of Coherent Magnon Modes in an Antiferromagnet, Phys. Rev. Lett. 127, 077202 (2021).

[41] M. Dressel and G. Grüner, *Electrodynamics of Solids* (Cambridge University Press, 2002).

[42] C. Lane and J.-X. Zhu, An ab initio study of electron-hole pairs in a correlated van der Waals antiferromagnet: $NiPS_3$, arXiv:2209.13051v2.

[43] I. J. Hamad, C. S. Helman, L. O. Manuel, A. E. Feiguin, and A. A. Aligia, Singlet polaron theory of low-energy optical excitations in $NiPS_3$, arXiv: 2404.12449.

[44] G. Jnawali, Y. Rao, H. Yan, and T. F. Heinz, Observation of a Transient Decrease in Terahertz Conductivity of Single-Layer Graphene Induced by Ultrafast Optical Excitation, Nano. Lett. 13, 524 (2013).

[45] A. J. Frenzel, C. H. Lui, Y. C. Shin, J. Kong, and N. Gedik, Semiconducting-to-Metallic Photoconductivity Crossover and Temperature-Dependent Drude Weight in Graphene, Phys. Rev. Lett. 113, 056602 (2014).

[46] C. H. Lui, A. J. Frenzel, D. V. Pilon, Y.-H. Lee, X. Ling, G. M. Akselrod, J. Kong, and N. Gedik, Trion-Induced Negative Photoconductivity in Monolayer MoS_2, Phys. Rev. Lett. 113, 166801 (2014).

[47] S. Y. Kim, T. Y. Kim, L. J. Sandilands, S. Sinn, M.-C. Lee, J. Son, S. Lee, K.-Y. Choi, W. Kim, B.-G. Park, C. Jeon, H.-D. Kim, C.-H. Park, J.-G. Park, S. J. Moon, and T. Noh, Charge-Spin Correlation in van der Waals Antiferromagnet $NiPS_3$, Phys. Rev. Lett. 120, 136402 (2018).

Supplemental Material for Long-lived population inversion in resonantly driven excitonic antiferromagnet

Jacob A. Warshauer,[1] Huyongqing Chen,[1] Daniel Alejandro Bustamante Lopez,[1] Qishuo Tan,[2] Jing Tang,[2] Xi Ling,[2,3,4] and Wanzheng Hu[1,3,4,*]

[1] *Department of Physics, Boston University, 590 Commonwealth Avenue, Boston, MA 02215, USA*

[2] *Department of Chemistry, Boston University, 590 Commonwealth Avenue, Boston, MA 02215, USA*

[3] *Division of Materials Science and Engineering, Boston University, 590 Commonwealth Avenue, Boston, MA 02215, USA*

[4] *Photonics Center, Boston University, 8 Saint Mary's St., Boston, MA 02215, USA*

[*] wanzheng@bu.edu

CONTENTS

S1. SAMPLE GROWTH AND OPTICAL CHARACTERIZATION

Single $NiPS_3$ crystals were synthesized using a chemical vapor transport method [1]. Precursors (the mole ratio of Ni:P:S = 1:1:3, in total of $\sim$ 1 g) and transport agent (I_2, $\sim$ 20 mg) were sealed into a quartz tube (pressure $< 10^{-5}$ hPa) and placed in a two-zone furnace at 650-500°C for a week. Raman and photoluminescenc (PL) measurements were conducted on Horiba-JY T64000 with a liquid nitrogen cooled CCD camera. Signals were collected through a $\times$50 objective and dispersed by an 1800 gr/mm grating for Raman spectroscopy, and by a 150 gr/mm grating for the PL measurement. A 532 nm laser generated by MSL-FN-532 (CNI) was used as the excitation light. Samples were placed inside a cryostat for temperature-dependent measurements. A linear polarizer and a half-wave plate were used in the collective path for the PL measurement.

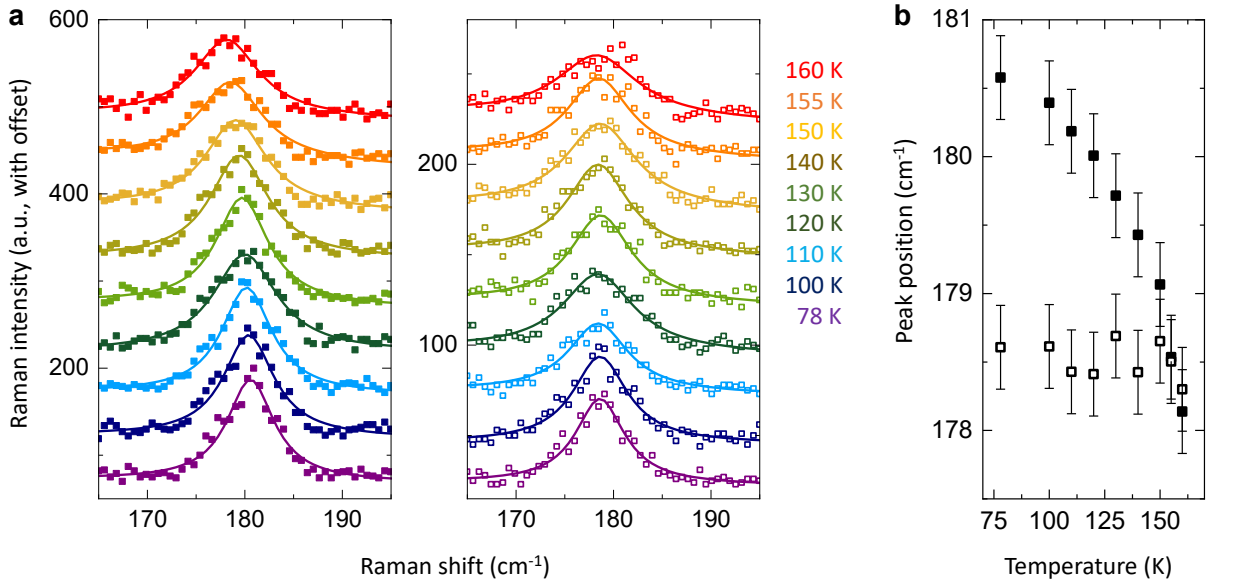

FIG. S1. **Characterizing the Néel temperature from a Raman phonon. a,** The 180 cm^{-1} Raman phonon measured with the parallel-polarization configuration (left panel) and the cross-polarization configuration (middle panel). The solid/open squares are the parallel/cross polarization data. The solid lines are the fits. **b,** Below the Néel temperature, the 180 cm^{-1} phonon frequencies measured by two configurations separate.

Figure S1a shows the Raman phonon near 180 cm^{-1} measured with the parallel- and cross-polarization configuration. This phonon is an optical indicator of the Néel temperature [2], that the frequency difference measured with orthogonal polarization configurations increases

with decreasing temperature below T_N (Fig. S1b).

S2. OPTICAL-PUMP-THZ-PROBE MEASUREMENT

The pump photon energies were selected by bandpass filters from the output of a 1 kHz 35 fs Ti-Sapphire laser. The actual pump spectra are shown as shaded peaks in Figure 1(a). The measured pulse duration for the parent laser pulse (centered at 1.55 eV) is 40 fs. The measured pulse durations for the three excitation pulses are 172 fs (for 1.476 eV), 171 fs (for 1.494 eV) and 121 fs (for 1.610 eV) (Fig. S2).

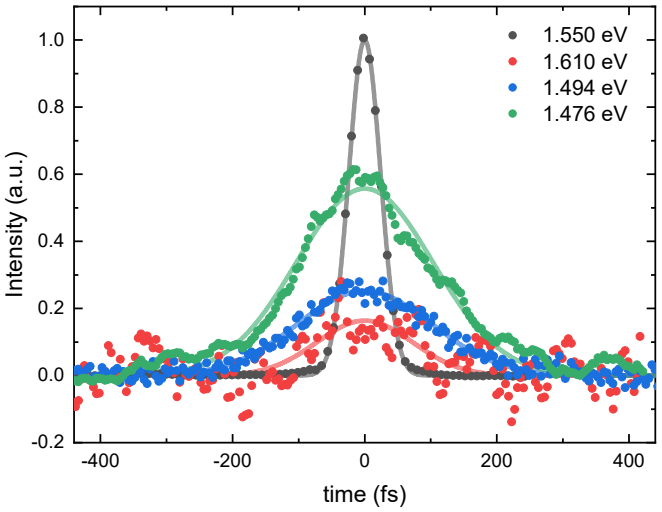

Center frequency (eV)	**Pulse Duration** (fs)
1.476	172
1.494	171
1.610	121
1.550	40

FIG. S2. **Measured auto-correlation signal of pump pulse through narrow-band optical filters. Figure,** Raw auto-correlation signal (scatter) and Gaussian fit (solid line) for each pump energy. Signal at 1.550 eV (black scatter) is the unfiltered pump pulse. **Table,** Pulse duration calculated for each pump energy. The unfiltered pump pulse has a 60 nm bandwidth. Each other pump energy is filtered using an 10 nm spectral width.

The incidence fluence was kept near 1 mJ/cm^2. The pump beam polarization was parallel to the a axis of $NiPS_3$. Broadband THz pulses were generated by laser-ionized plasma from the same 35 fs Ti-Sapphire laser. The reflected THz signal were detected by electrooptical sampling in a 1 mm thick ZnTe crystal. A long-pass filter was used to remove the scattered pump photons. The THz transient and the pump-induced change were simultaneously measured by two lock-in amplifiers.

The normalized spectrally-integrated pump-induced change in the THz field amplitude

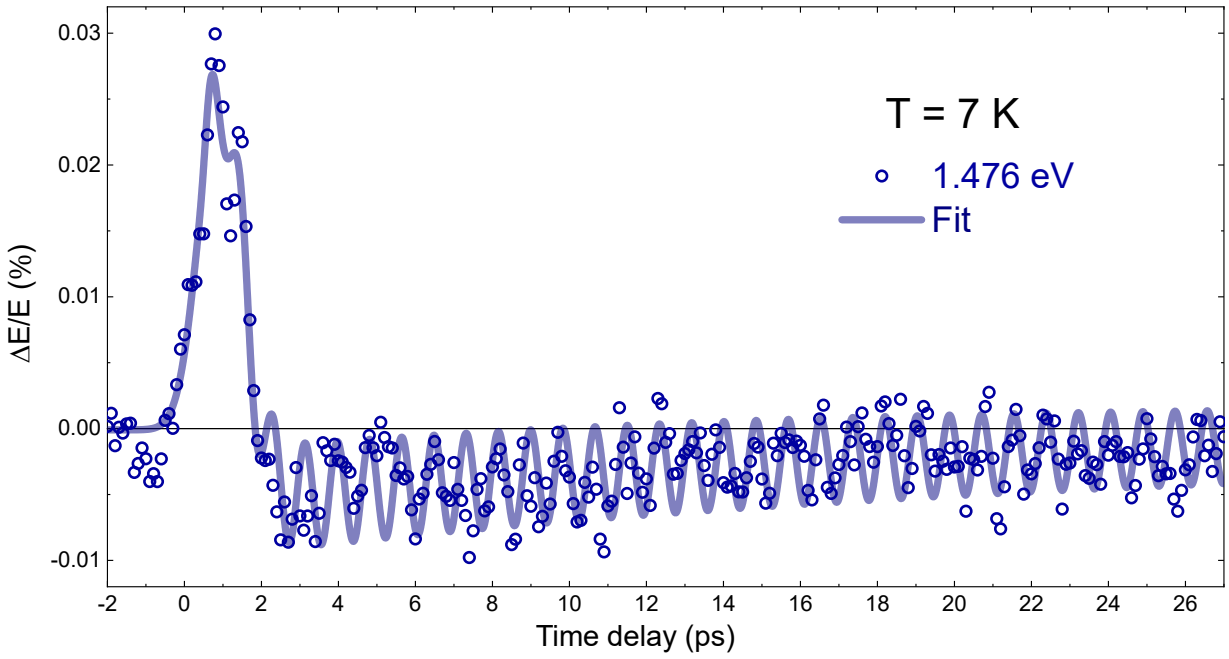

FIG. S3. **Spectrally-integrated response with resonant pumping at peak I.** Normalized pump-induced change in the THz electric field at 7 K with 1.476 eV pumping. This is the same data set as Fig. 2a plotted over a broader time window.

$(\Delta E/E)$ is shown in Fig. S3, which is the same data as Fig. 2a in the main text but plotted over an extended time window. The magnon mode is seen as a fast oscillation of $\Delta E/E$. A 17 ps lifetime is used to fit the negative $\Delta E/E$ response, and a 70 ps lifetime is used to fit the magnon oscillation.

S3. ESTIMATED PUMP-INDUCED HEATING

A basic model for absorbed energy from the pump laser source can be written as $E_p^a = \phi_p A_p(1-e^{-\alpha\delta_p})$, with ϕ_p as pump fluence, A_p as pump spot area, δ_p as the penetration depth at the pump frequency, and α being the absorption coefficient calculated from a fit to the absorption edge.

We set the absorbed pump energy equal to the energy taken to increase from the starting temperature T_0 to the final temperature T_1:

$$E_p^a = \int_{T_0}^{T_1} M_e C_v(T) dT \tag{1}$$

where M_e is the excited mass and C_v is the heat capacity [3, 4]. Solving this for T_1 gives the

resulting temperature due to pump heating, as shown in Table S1. A significant pump-induced heating and the weak THz reflection signal for insulating $NiPS_3$ challenge the magnon detection, in particular for the 1.610 eV pumping case.

Pump energy (eV)	**ΔT** (K)
1.476	20
1.494	37
1.610	78

TABLE S1. Effective pump pulse heating of sample. Starting temperature $T_0 = 7$ K.

S4. FREQUENCY-RESOLVED RESPONSE AND THE DRUDE-LORENTZ FIT

In the frequency-resolved optical pump and THz probe experiment, the light-induced change of the complex THz electric field $\Delta\tilde{E}(\omega)$ is measured for each pump-probe time delay τ. In the case where the pump penetration depth is orders of magnitude smaller than the probe penetration depth, the measured $\Delta\tilde{E}(\omega)$ can be modeled as a signal coming from a thin film of photo-excited layer on top of a semi-infinite layer which remains the equilibrium optical properties [5]. In the case of normal incidence, the light-induced change in complex optical conductivity at time delay τ can be evaluated by:

$$\Delta\tilde{\sigma}(\omega,\tau) = \frac{1}{377\delta_p}\frac{\frac{\Delta\tilde{E}(\omega,\tau)}{\tilde{E}(\omega)}\left(\tilde{n}^2(\omega)-1\right)}{\frac{\Delta\tilde{E}(\omega,\tau)}{\tilde{E}(\omega)}\left(1-\tilde{n}(\omega)\right)+2} \tag{2}$$

where δ_p is the pump penetration depth, $\frac{\Delta\tilde{E}(\omega,\tau)}{\tilde{E}(\omega)}$ is the light-induced change of the complex THz electric field at time delay τ normalized by the equilibrium THz electric field, and $\tilde{n}(\omega)$ is the equilibrium complex refractive index. Since the equilibrium refractive index is nearly featureless in the THz region [4], a frequency-independent equilibrium optical response was used to evaluate the light-induced change in the complex optical conductivity. The $NiPS_3$ samples used in this study are transparent in the THz region with a typical thickness of 0.4 mm. The pump penetration depths for all pump wavelengths are evaluated from the equilibrium optical data [6, 7]. The results are shown in Table S2.

A Drude-Lorentz model was used to fit the transient changes in the optical conductivity $\Delta\sigma_1(\omega)$ and $\Delta\sigma_2(\omega)$ simultaneously. In the Drude-Lorentz model [8], the complex optical

Pump energy (eV)	**T** (K)	$\delta_{\mathbf{p}}$ (μm)
1.476	7	5.0
1.494	7	4.9
1.610	7	0.9
1.476	295	0.9

TABLE S2. Pump penetration depths.

conductivity is

$$\tilde{\sigma}(\omega)^{DL} = \sum_i \frac{\omega_{p,i}^2}{4\pi} \frac{\omega}{i(\omega_i^2 - \omega^2) + \omega\Gamma_i} \tag{3}$$

where $\omega_{p,i}^2$ is the oscillator strength for the i-th Drude/Lorentz term, and ω_i (Γ_i) is the center frequency (scattering rate) for the Drude/Lorentz term. For the Drude term, $\omega_i = 0$.

The light-induced change is defined as $\Delta\tilde{\sigma}(\omega) = \tilde{\sigma}(\omega)^{\mathrm{DL}} - \tilde{\sigma}(\omega)^{\mathrm{equilibrium}}$. For resonant pumping at the exciton energy (peak I, 1.476 eV), we used Equ. 3 to fit $\Delta\sigma_1(\omega)$ and $\Delta\sigma_2(\omega)$ simultaneously with one Drude term and one inverted Lorentz term. Here the inverted Lorentz term has a negative ω_p^2. The results are shown in Fig. S4. For all other pumping situations ($E_{pump} = 1.494$ eV or 1.610 eV at $T = 7$ K, or $E_{pump} = 1.476$ eV at $T = 295$ K), only one Drude term was used to fit $\Delta\sigma_1(\omega)$ and $\Delta\sigma_2(\omega)$ simultaneously.

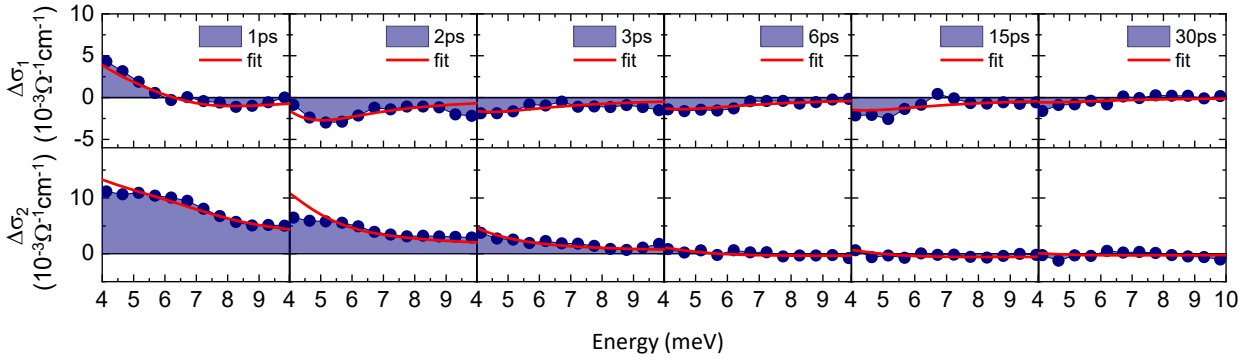

FIG. S4. **Frequency-resolved transient changes in complex optical conductivity at 7 K.** Resonant pumping at the exciton energy (peak I, 1.476 eV) results in a long-lived transient suppression in σ_1 and an increase in σ_2. The solid circles present the data, and the red curves are fits. For all time delays, $\Delta\sigma_1(\omega)$ and $\Delta\sigma_2(\omega)$ are fit simultaneously with one Drude term and one inverted Lorentz term.

S5. ROOM TEMPERATURE RESPONSE

Due to a strong temperature dependence of the 2.2 eV charge transfer gap [6, 9], the absorption onset red-shifts with increasing temperature significantly. At room-temperature, 1.476 eV pumping is above the absorption onset [7]. Therefore, pumping at 1.476 eV induces a large amount of hot carriers. Figure S5a shows the spectrally-integrated response, $\Delta E/E$, which is similar to Fig. 2b in the main text. Figure S5b-e illustrate the complex optical conductivity change at various pump-probe time delays. In stark contrast to the 7 K data (main text Fig. 2a), at room temperature the light-induced change $\Delta\sigma_1(\omega)$ is always positive. A single Drude term is used to fit $\Delta\sigma_1(\omega)$ and $\Delta\sigma_2(\omega)$ simultaneously for each time delay. The Drude oscillator strength, ω_{pD}^2, is shown in Fig. S5f. It is fit by a single exponential decay with a 2 ps time constant. This is very close to the 2.4 ps lifetime of the Drude term in the 7 K data. Note that at room temperature both the Drude scattering rate (the width of the Drude peak in $\sigma_1(\omega)$) and the plasma frequency ω_p are significantly larger than the 7 K case, which is due to the red-shifted absorption onset.

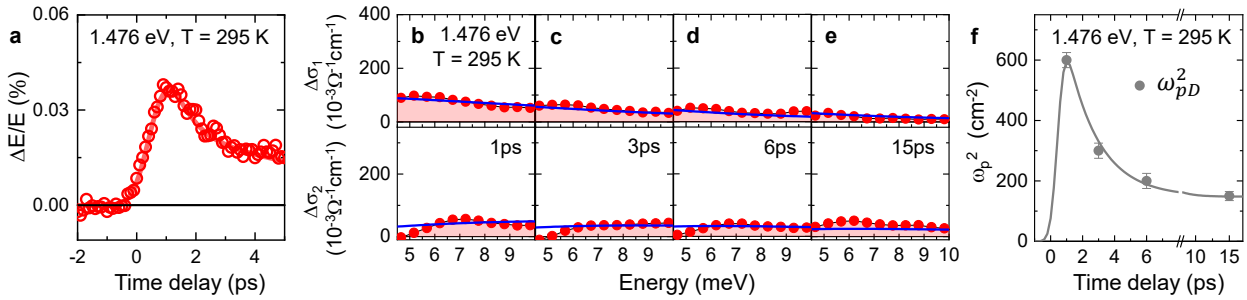

FIG. S5. **Light-induced change in complex optical conductivity at 295 K with 1.476 eV pumping.** **a,** Spectrally-integrated transient response (open circles) with exponential fit (solid line). **b-e,** All time delays show a Drude-like response with positive $\Delta\sigma_1$ and positive $\Delta\sigma_2$. The solid circles present the data, and the blue curves are fits. Only one Drude term is used in the fit. **f,** Time dependence of the Drude oscillator strengths ω_{pD}^2 used to fit **b-e**. The thin solid line is an exponential decay fit.

S6. FLUENCE DEPENDENCE OF POPULATION INVERSION

A pump-induced negative photoconductivity in the THz energy regime is observed in $NiPS_3$ when pumping at 1.476 eV. No suppression is seen at the lowest fluence measured, and a saturating behavior is noted at higher fluences. We analyze this result with population inversion between exciton levels using a simple four-level optical transition model. We model the rate of change of level populations using Einstein coefficients for absorption, spontaneous emission, and stimulated emission. In this system, the population inversion we describe occurs between the first (E_1, population N_1) and second (E_2, population N_2) excited levels. The rate equation for the second excited level can be written as

$$\begin{aligned}\frac{dN_2}{dt} &= B_{12}N_1\rho(\omega_{12}) - B_{21}N_2\rho(\omega_{12}) - A_{21}N_2 + B_{02}N_0\rho(\omega_{02}) \\ &\quad - B_{20}N_2\rho(\omega_{02}) - A_{20}N_2 - B_{23}N_2\rho(\omega_{23}) + B_{32}N_3\rho(\omega_{23}) + A_{32}N_3,\end{aligned} \tag{4}$$

where $B_{E_i \to E_{i+1}}$ is the Einstein coefficient for absorption of a photon with energy $E_{i+1} - E_i$ inducing transitions to higher energy, $B_{E_i \to E_{i-1}}$ is the Einstein coefficient for stimulated emission leading to transitions to lower energy with the coherent emission of a photon, $A_{E_i \to E_{i-1}}$ is the rate of spontaneous decay to lower energy level as a result of the spontaneous emission of a photon, and $\rho(\omega)$ is the energy density of the electromagnetic field [10].

We will model our system as a steady state due to the long lived nature of our observed phenomena. In this case, we can take $dN_i/dt = 0$ and $B_{ij} = B_{ji}$ [11]. We also will take advantage of the relatively closely spaced energies of the intraexciton transitions, allowing our pump to excite all transitions from E_0 to excited levels in this model. This system of equations following from Equ. 4 allow us to find the rate conditions allowing population inversion between exciton levels as well as the fluence dependence of the population inversion.

Population inversion between E_2 and E_1 is defined as the condition $N_2 > N_1$. Assuming similar Einstein coefficients of absorption, $N_2 > N_1$ can be realized for rates of spontaneous decay following $A_{32} > A_{21}, A_{10}$. We find that the fluence dependence in this regime shows a threshold at which population inversion does not occur below. Above this threshold, population inversion should saturate with high fluence as fewer states are available at the upper excited energy levels [10]. Using the simple model within this regime, we can fit the fluence dependence of the suppression of spectral weight seen at 7 K when pumping with 1.476 eV (Fig. S6).

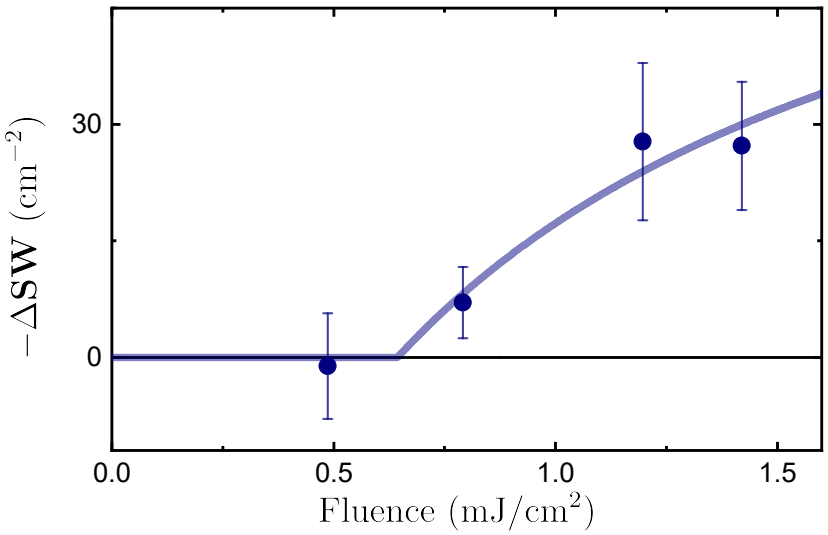

FIG. S6. **Transient change in spectral weight as a function of incident pump fluence.** Change in spectral weight at 3.0 ps pump-probe delay calculated by the integration of the transient change in optical conductivity, $\mathbf{\Delta SW} = \frac{120}{\pi}\int_{\omega_0}^{\omega_1}\Delta\sigma_1(\omega)d\omega$, over the energy region from $\omega_0 = 3.81$ meV to $\omega_1 = 10.48$ meV. The data was taken under 1.476 eV optical pumping at 7 K. Fluence dependence follows the threshold-saturation behavior expected for population inversion between excited energy levels.

S7. THEORETICAL CALCULATION ON THE MAGNON MODES

The Hamiltonian for $NiPS_3$ is

$$\mathcal{H} = J_1\sum_{\langle i,j\rangle}\mathbf{S}_i\cdot\mathbf{S}_j + J_2\sum_{\langle\langle i,j\rangle\rangle}\mathbf{S}_i\cdot\mathbf{S}_j + J_3\sum_{\langle\langle\langle i,j\rangle\rangle\rangle}\mathbf{S}_i\cdot\mathbf{S}_j + \sum_i\left(D_xS_{i,x}^2 + D_zS_{i,z}^2\right) \tag{5}$$

with x parallel to the aligned moment direction and z normal to both this direction and b; J is the exchange interaction, with magnetic exchange up to the third-nearest neighbor (Fig. S7), and D is the anisotropy strength.

The Hamiltonian can be rewritten as

$$\mathcal{H} = J\mathbf{S}_1\cdot\mathbf{S}_2 + \sum_{i\in\{1,2\}}\left(D_xS_{i,x}^2 + D_zS_{i,z}^2\right) \tag{6}$$

where $J = J_1 + 4J_2 + 3J_3$.

The Landau-Lifshitz-Gilbert equations are

$$\frac{d\mathbf{S}_\sigma}{dt} = \frac{\gamma_{\text{el}}}{1+\kappa_{\text{el}}}\left[\mathbf{S}_\sigma \times \mathbf{B}_\sigma^{\text{eff}} - \frac{\kappa_{\text{el}}}{|\mathbf{S}_\sigma|}\mathbf{S}_\sigma \times \left(\mathbf{S}_\sigma \times \mathbf{B}_\sigma^{\text{eff}}\right)\right] \tag{7}$$

where

$$\mathbf{B}_\sigma^{\text{eff}} = -\frac{1}{\gamma_{\text{el}}}\frac{\partial H}{\partial \mathbf{S}_\sigma} = \mathbf{B} - \frac{1}{\gamma_{\text{el}}}\left(J\mathbf{S}_{\sigma'} + 2D_x S_{\sigma,x}\hat{\mathbf{x}} + 2D_z S_{\sigma,z}\hat{\mathbf{z}}\right) \tag{8}$$

$\mathbf{B}$ is the external magnetic field, and $\sigma, \sigma' \in \{1, 2\}$, with $\sigma \neq \sigma'$.

If $\mathbf{B} = B\hat{\mathbf{y}}$, then the first-order corrections due to the magnetic field can be written in the frequency domain as

$$S_x^{(1)}(\omega) = 0 \tag{9a}$$

$$S_y^{(1)}(\omega) = \frac{2\gamma_{\text{el}} S^2\hbar^2(D_z - D_x)}{\Delta_1(\omega)}B(\omega) \tag{9b}$$

$$S_z^{(1)}(\omega) = \frac{\gamma_{\text{el}} S\hbar i\omega}{\Delta_1(\omega)}B(\omega) \tag{9c}$$

where $\Delta_1(\omega) = \Omega_1^2 - \omega^2 + i\kappa\omega$, with frequency $\Omega_1 = 2S\hbar\sqrt{(D_x - D_z)(D_x - J)}$ and linewidth $\kappa = 2\kappa_{\text{el}} S\hbar\,(J + D_z - 2D_x)$, such that $S_{1,x}^{(1)} = S_{2,x}^{(1)} = 0$, $S_{1,y}^{(1)} = S_{2,y}^{(1)} = S_y^{(1)}$, and $S_{1,z}^{(1)} = -S_{2,z}^{(1)} = S_z^{(1)}$.

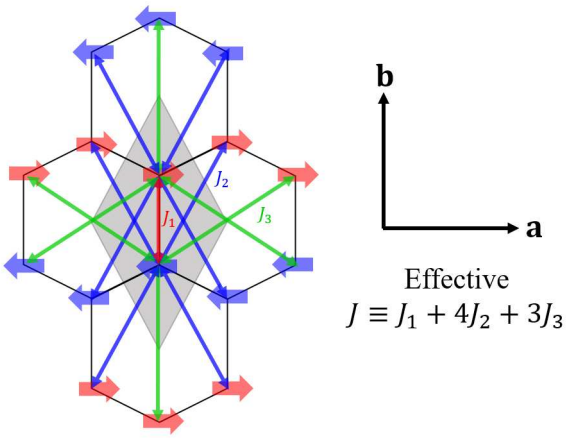

FIG. S7. The magnetic structure of $NiPS_3$. Magnetic exchange up to the third-nearest neighbor is shown.

On the other hand, if $\mathbf{B} = B\hat{\mathbf{z}}$, then

$$S_x^{(1)}(\omega) = 0 \tag{10a}$$

$$S_y^{(1)}(\omega) = -\frac{\gamma_{\rm el} S\hbar i\omega}{\Delta_2(\omega)} B(\omega) \tag{10b}$$

$$S_z^{(1)}(\omega) = -\frac{2\gamma_{\rm el} S^2\hbar^2 D_x}{\Delta_2(\omega)} B(\omega) \tag{10c}$$

where $\Delta_2(\omega) = \Omega_2^2 - \omega^2 + i\kappa\omega$, with frequency $\Omega_2 = 2S\hbar\sqrt{D_x(D_x - D_z - J)}$ and linewidth $\kappa = 2\kappa_{\rm el} S\hbar\,(J + D_z - 2D_x)$, such that $S_{1,x}^{(1)} = S_{2,x}^{(1)} = 0$, $S_{1,y}^{(1)} = -S_{2,y}^{(1)} = S_y^{(1)}$, and $S_{1,z}^{(1)} = S_{2,z}^{(1)} = S_z^{(1)}$.

Parameter	**Value**
S	1
J_1	-2.6 meV
J_2	0.2 meV
J_3	13.5 meV
J	38.7 meV
D_x	-0.01 meV
D_z	0.21 meV
$\kappa_{\rm el}$	2.4×10^{-4}

TABLE S3. Values for $NiPS_3$ as given in Ref. [12].

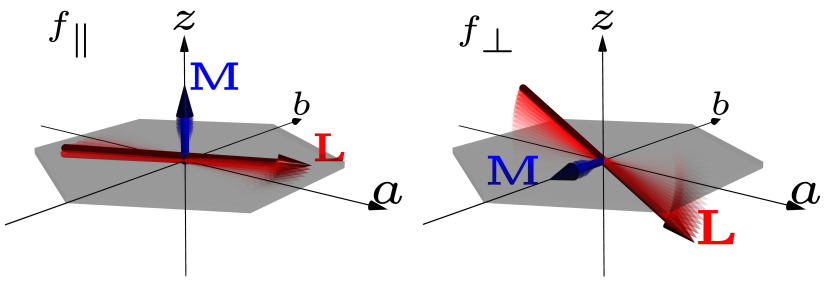

FIG. S8. **Low- and high-frequency magnon modes in $NiPS_3$.** The ferromagnetic $\mathbf{M} = \mathbf{S}_1 + \mathbf{S}_2$ and antiferromagnetic $\mathbf{L} = \mathbf{S}_1 - \mathbf{S}_2$ vectors are shown. The low-frequency mode is characterized by transient ΔM_z and ΔL_y, while the high-frequency mode has ΔM_y and ΔL_z. Here $f_{\parallel} = \Omega_2/(2\pi) = 0.302\,\text{THz}$, and $f_{\perp} = \Omega_1/(2\pi) = 1.411\,\text{THz}$.

Therefore, the magnon has two eigenfrequencies, $\Omega_1/(2\pi) = 1.411$ THz and $\Omega_2/(2\pi) = 0.302$ THz (see Fig. S8) for the parameters in Table S3. Furthermore, it has a lifetime of $2/\kappa = 70.45$ ps.

[1] X. Wang, J. Cao, Z. Lu, A. Cohen, H. Kitadai, T. Li, Q. Tan, M. Wilson, C. H. Lui, D. Smirnov, S. Sharifzadeh, and X. Ling, Spin-induced linear polarization of photoluminescence in antiferromagnetic van der Waals crystals, Nature Materials **20**, 964– (2021).

[2] K. Kim, S. Y. Lim, J.-U. Lee, S. Lee, T. Y. Kim, K. Park, G. S. Jeon, C.-H. Park, J.-G. Park, and H. Cheong, Suppression of magnetic ordering in XXZ-type antiferromagnetic monolayer $NiPS_3$, Nature Communications **10**, 345 (2019).

[3] M. Šiškins, M. Lee, S. M. nas Valero, E. Coronado, Y. M. Blanter, H. S. J. van der Zant, and P. G. Steeneken, Magnetic and electronic phase transitions probed by nanomechanical resonators, Nature Communications **11**, 2698 (2020).

[4] C. A. Belvin, E. Baldini, I. O. Ozel, D. Mao, H. C. Po, C. J. Allington, S. Son, B. H. Kim, J. Kim, I. Hwang, J. H. Kim, J.-G. Park, T. Senthil, and N. Gedik, Exciton-driven antiferromagnetic metal in a correlated van der Waals insulator, Nature Communications **12**, 4837 (2021).

[5] D. Fausti, R. I. Tobey, N. Dean, S. Kaiser, A. Dienst, M. C. Hoffmann, S. Pyon, T.Takayama, H. Takagi, and A. Cavalleri, Light-Induced Superconductivity in a Stripe-Ordered Cuprate, Science **331**, 189 (2011).

[6] S. Y. Kim, T. Y. Kim, L. J. Sandilands, S. Sinn, M.-C. Lee, J. Son, S. Lee, K.-Y. Choi, W. Kim, B.-G. Park, C. Jeon, H.-D. Kim, C.-H. Park, J.-G. Park, S. J. Moon, and T. Noh, Charge-Spin Correlation in van der Waals Antiferromagnet $NiPS_3$, Phys. Rev. Lett. **120**, 136402 (2018).

[7] C.-H. Ho, T.-Y. Hsu, and L. C. Muhimmah, The band-edge excitons observed in few-layer $NiPS_3$, npj 2D Materials and Applications **5**, 8 (2021).

[8] M. Dressel and G. Grüner, *Electrodynamics of Solids* (Cambridge University Press, 2002).

[9] T. Klaproth, S. Aswartham, Y. Shemerliuk, S. Selter, O. Janson, J. van den Brink, B. Büchner, M. Knupfer, S. Pazek, D. Mikhailova, A. Efimenko, R. Hayn, A. Savoyant, V. Gubanov, and A. Koitzsch, Origin of the Magnetic Exciton in the van der Waals Antiferromagnet $NiPS_3$, Phys. Rev. Lett. **131**, 256504 (2023).

[10] R. D. Guenther and D. Steel, *Encyclopedia of Modern Optics* (Academic Press, San Diego, CA, 2018).

[11] J. T. Verdeyen, *Laser Electronics* (Presntice-Hall, 1995).

[12] A. R. Wildes, J. R. Stewart, M. D. Le, R. A. Ewings, K. C. Rule, G. Deng, and K. Anand, Magnetic dynamics of $NiPS_3$, Phys. Rev. B **106**, 174422 (2022).